Journal of Materials Chemistry A

PAPER

View Article Online
View Journal | View Issue

Cite this: J. Mater. Chem. A, 2016, 4, 6411

Symmetric pseudocapacitors based on molybdenum disulfide (MoS_2)-modified carbon nanospheres: correlating physicochemistry and synergistic interaction on energy storage†

Tobile N. Y. Khawula,[a] Kumar Raju,[b] Paul J. Franklyn,[c] Iakovos Sigalas[a] and Kenneth I. Ozoemena*[bc]

Molybdenum disulfide-modified carbon nanospheres (MoS_2/CNS) with two different morphologies (spherical and flower-like) have been synthesized using hydrothermal techniques and investigated as symmetric pseudocapacitors in an aqueous electrolyte. The physicochemical properties of these MoS_2/CNS layered materials have been investigated using surface area analysis (BET), scanning electron microscopy (SEM), transmission electron microscopy (TEM), X-ray diffraction (XRD), Raman, Fourier transform infrared (FTIR) spectroscopy, and advanced electrochemistry, including cyclic voltammetry (CV), galvanostatic cycling with potential limitation (GCPL), long-hour voltage-holding tests, and electrochemical impedance spectroscopy (EIS). The two different MoS_2/CNS layered materials exhibit unique differences in morphology, surface area, and structural parameters, which have been correlated with their electrochemical capacitive properties. The flower-like morphology (f-MoS_2/CNS) shows lattice expansion (XRD), large surface area (BET analysis), and small-sized nanostructures (corroborated by the larger FWHM of the Raman and XRD data). In contrast to the f-MoS_2/CNS, the spherical morphology (s-MoS_2/CNS) shows lattice contraction and small surface area with relatively large-sized nanostructures. The presence of CNS on the MoS_2 structure leads to slight softening of the characteristic Raman bands (E^1_{2g} and A_{1g} modes) with larger FWHM. MoS_2 and its CNS-based composites have been tested in symmetric electrochemical capacitors in an aqueous 1 M Na_2SO_4 solution. CNS improves the conductivity of the MoS_2 and synergistically enhances the electrochemical capacitive properties of the materials, especially the f-MoS_2/CNS-based symmetric cells (most notably, in terms of capacitance retention). The f-MoS_2/CNS-based pseudocapacitor shows a maximum capacitance of 231 F g^{-1}, with high energy density 26 W h kg^{-1} and power density 6443 W kg^{-1}. For the s-MoS_2/CNS-based pseudocapacitor, the equivalent values are 108 F g^{-1}, 7.4 W h kg^{-1} and 3700 W kg^{-1}. The high-performance of the f-MoS_2/CNS is consistent with its physicochemical properties as determined by the spectroscopy and microscopy data. These findings have opened doors for further exploration of the synergistic effects between MoS_2 graphene-like sheets and CNS for energy storage.

Received 5th January 2016
Accepted 23rd March 2016

DOI: 10.1039/c6ta00114a

www.rsc.org/MaterialsA

Introduction

Pseudocapacitors are redox-based electrochemical capacitors (ECs). Unlike their counterparts, the electrical double layer capacitors (EDLC) that only use carbon materials as electrode materials, pseudocapacitors employ redox-active materials such as conducting polymers, metal oxides and metal sulphides.[1–4] Unlike batteries with high energy densities, ECs are characterized by their high power characteristics, which make them very attractive for several technologies and devices that require high-power applications (*i.e.*, the ability to release energy pulses in a very short time, in a few seconds) such as in regenerative braking energy systems in vehicles and metro-rails, "stop–start" applications in modern cars, uninterrupted power supply (UPS), emergency doors in aircrafts, and escalators in buildings.[5,6]

One of the emerging high-power supercapacitor electrode materials is molybdenum disulfide (MoS_2), a member of the transition-metal dichalcogenides (TMDs). MoS_2 has found applications in electrochemical devices, hydrogen storage, catalysis, capacitors, solid lubricants, and intercalation hosts.[7,8]

[a]School of Chemical and Metallurgical Engineering, University of the Witwatersrand, PO Wits 2050, Johannesburg, South Africa

[b]Energy Materials, Materials Science and Manufacturing, Council for Scientific and Industrial Research (CSIR), Pretoria 0001, South Africa. E-mail: kozoemena@csir.co.za

[c]Molecular Sciences Institute, School of Chemistry, University of the Witwatersrand, PO Wits 2050, Johannesburg, South Africa

† Electronic supplementary information (ESI) available. See DOI: 10.1039/c6ta00114a

MoS_2 is a layered-structured material with close relationship to graphene, characterized by a sheet-like morphology. The Mo layer is sandwiched between two S layers and the triple layers are stacked and held together by weak van der Waals interactions.[2,9–11] Due to its higher intrinsic fast ionic conductivity (than oxides) and higher theoretical capacity (than graphite), MoS_2 continues to attract a lot of attention, particularly in supercapacitors.[2,7,12] Soon and Loh[13] have pointed out the use of MoS_2 as an electrode material for supercapacitors, and the results suggest that the supercapacitor performance of MoS_2 is comparable to that of carbon nanotube (CNT) array electrodes. In addition to double-layer capacitance, diffusion of the ions into the MoS_2 at slow scan rates obtains faradaic capacitance. Analogous to Ru in RuO_2, the Mo central atom displays a range of oxidation states from +2 to +6. This plays an important role in enhancing charge storage capabilities.[14] However, the electronic conductivity of MoS_2 is still lower compared to graphite and the specific capacitance of MoS_2 is still very limited when used alone for energy storage applications.[12,13,15] As evident in several reports, there is the need to improve the capacitance of MoS_2 with conductive materials such as CNT,[12] polyaniline (PANI),[2] polypyrrole (PPy),[9] and reduced graphene (RGO).[11] In a review by Márquez *et al.*,[16] carbon nanospheres (CNS) were described as good candidates for catalytic and adsorption applications and their unclosed graphitic flakes provide the necessary 'dangling bonds' that could enhance surface reactions. CNS has also been used to enhance the conductivity of the battery cathode material, $LiFePO_4$.[17]

To the best of our knowledge, the supercapacitive properties of MoS_2 have only been investigated in half-cells (*i.e.*, 3-electrode systems), which creates a huge knowledge gap on the true behavior of the electrode material when used in full-cells (2-electrode systems). Moreover, there is no literature on the effect of CNS on the supercapacitance of MoS_2. Pseudocapacitors usually suffer from poor electrical conductivity and irreversible redox-activity, thereby leading to gradual loss of capacitance. To tackle the abovementioned challenges, this study adopted two different synthesis protocols to prepare MoS_2 and MoS_2/CNS composites with different physicochemistries (*i.e.*, spherical and flower-like morphologies, structure, porous textures and electrochemistry) and then used them to fabricate symmetric pseudocapacitors. We clearly show that the pseudocapacitive properties of the MoS_2/CNS (especially, in terms of cycling stability and electronic conductivity) are intrinsically linked to the presence of CNS.

Experimental procedure

Materials

Sodium molybdate dihydrate, $Na_2MoO_4 \cdot 2H_2O$ (Analytical Reagent BDH chemicals Ltd, Poole England), thiourea (CH_4N_2S, Sigma-Aldrich Inc., USA), polyethylene glycol 1000 (PEG-1000, Fluka Analytical, Germany), L-cysteine ($C_3H_7NO_2S$, Sigma-Aldrich Inc., USA). Hydrochloric acid (HCl, 32%), acetone (C_3H_6O) and absolute ethanol (C_2H_6O) were purchased from Associated Chemical Enterprises, in Johannesburg. All chemicals had purity higher than 98.99%. Distilled de-ionised water (18 MΩ cm) used in this study was obtained from the School of Chemistry at the University of the Witwatersrand.

Synthesis

Spherical MoS_2. Spherical MoS_2 was synthesized using a well-established method by Huang *et al.*,[18] as follows: 0.31 g $Na_2MoO_4 \cdot 2H_2O$ were dissolved in 30 mL deionized water. After adjusting the pH value to 6.5 with 12 M HCl, 0.82 g L-cysteine was added and the mixture was diluted with water to 35 mL and then the solution was rapidly stirred for about an hour. Subsequently, the mixture was transferred into a 40 mL Teflon-lined stainless steel autoclave and heated at 180 °C for 48 hours. The black MoS_2 precipitate was cooled naturally to room temperature, collected by centrifugation, washed with distilled water and absolute ethanol in three cycles and then dried in vacuum at 60 °C for 24 hours. For simplicity, the obtained spherical material (as evident from SEM and TEM images) is abbreviated as s-MoS_2.

Flower-like MoS_2. Flower-like MoS_2 was synthesized as suggested by Wang *et al.*[19] 1.21 g $Na_2MoO_4 \cdot 2H_2O$ and 1.56 g thiourea powders were mixed together in 30 mL deionised water, and 0.14 g PEG-1000 were added. The resulting mixture was transferred to a Teflon cup of capacity 40 mL and heated in a stainless steel autoclave at 180 °C for 24 h. After cooling naturally to room temperature, the black MoS_2 precipitate was collected by centrifugation, washed with distilled water and absolute ethanol in three cycles, and then dried under vacuum at 60 °C for 24 h.[19] The obtained flower-like material (as evident from SEM and TEM images) is abbreviated herein as f-MoS_2.

Carbon nanospheres (CNS). Carbon nanospheres (CNS) were obtained using the established method by Dlamini *et al.*[20] In brief, sucrose solution (0.3 M) was transferred into a 100 mL Teflon-lined stainless steel autoclave and heated at 150 °C for 5 hours. The reaction was then left to cool at room temperature. At this stage, the black precipitate that formed was purified by Soxhlet extraction, washed with ethanol and water and then dried at 80 °C in an oven.

The CNS-modified spherical MoS_2 (abbreviated herein as s-MoS_2/CNS) composite was prepared as follows. First, 0.028 g CNS were ultrasonically dispersed in 20 mL deionized water. Then, 0.30 g $Na_2MoO_4 \cdot 2H_2O$ were added and ultrasonically dispersed for 30 min. After adjusting the pH value to 6.5 with 12 M HCl, 0.80 g L-cysteine was added. The resultant mixture was diluted with water to 30 mL and rapidly stirred for about 1 h. The mixture was then transferred into a 40 mL Teflon cup and heated in a stainless steel autoclave at 180 °C for 36 h. Upon completion, the product was cooled naturally to room temperature, the s-MoS_2/CNS composite was collected by filtration, washed with distilled water and acetone several times, and finally dried in the oven at 80 °C for 24 h.

The CNS-modified flower-like MoS_2 composite (abbreviated herein as f-MoS_2/CNS) was prepared as follows. 1.21 g $Na_2MoO_4 \cdot 2H_2O$ were added to the sonicated CNS in 20 mL deionised water and further sonicated for 30 min. Then, 1.56 g thiourea and 0.28 g PEG-1000 were added to the solution and the mixture diluted to 30 mL before heating to 180 °C using

a Teflon-lined stainless steel autoclave for 36 h. Upon completion, the product was cooled naturally to room temperature, the f-MoS_2/CNS composite was collected by filtration, washed with distilled water and acetone several times, and finally dried in oven at 80 °C for 24 h. To homogenize the as-synthesized materials and further promote crystallization, the as-synthesized materials were annealed in a horizontal furnace with a quartz tube at 900 °C under a flow of nitrogen at a rate of 100 mL min^{-1} for 4 h.

Characterization techniques

The XRD patterns of the as-prepared MoS_2 and MoS_2/CNS nanopowders were obtained from a DMax/2500PC diffractometer using Co Kα radiation ($K = 1.5418$ Å) at 40 kV, 100 mA and a 2θ range of 10–90°. The FTIR spectra were obtained using a Bruker Tensor 27 FTIR spectrometer equipped with ZnSe crystal that absorbs strongly below 500 cm^{-1}. FTIR spectra were obtained in the range of 550–4000 cm^{-1}; a single beam measurement as the background spectrum was acquired prior to running the actual sample. Raman measurements were carried out in air using a Horiba Jobin Yvon spectrometer equipped with an Olympus BX40 microscope attachment to focus the laser beam on a small selected area of the sample, a 30 mW green argon laser ($\lambda = 514$ nm) as the excitation source, and a 1800 lines per mm grating monochromator with liquid nitrogen-cooled CCD. The BET (Brunauer, Emmett and Teller) measurements were performed to determine the specific surface area and pore size of the nano-sheets using a Micromeritics TriStar II instrument. The SEM images were obtained using a JEOL-JSM 7500F scanning electron microscope operated at 2.0 kV and a FEI Nova Nanolab 600 SEM. TEM images were obtained from a FEI Tecnai T12 microscope operated at an acceleration voltage of 120 kV. Elemental composition was obtained using the Oxford INCA EDS software on the SEM.

Fabrication of the symmetric pseudocapacitor and electrochemical measurements

Symmetric pseudocapacitive properties of the materials were investigated using Swagelok cells (MTI, Inc., USA). Nickel foam (Celmet: thickness = 1.6 mm, surface area 7500 m^2, cell size = 0.5 mm, 48–52 cells per inch) was used as substrate and current collector in the fabrication of the symmetric pseudocapacitors. Before use, the nickel foam was thoroughly cleaned by sonicating in 1 M HCl solution for 30 min, washing with copious amount of distilled water, and finally drying under vacuum. A 1 M Na_2SO_4 solution was used as the electrolyte, whereas a porous filter paper (Whatman®) served as the separator. The electrode materials were prepared by first thoroughly mixing the active materials, either MoS_2/CNS or MoS_2, carbon black as the conducting agent, and polyvinylidene fluoride (PVDF) as the binder (80 : 15 : 5 weight ratio) with a few drops of anhydrous *N*-methyl-2-pyrrolidone (NMP) using pestle and mortar, to produce a homogeneous paste. The resulting slurry was coated onto the nickel foam substrate with a spatula. The electrode was then dried at 60 °C overnight in a vacuum oven. The mass of the active material on the nickel foam was between 5 and 20 mg. For complete impregnation, the assembled cells were left for 12 hours prior to testing. The measurements were carried out in 1 M Na_2SO_4 aqueous electrolyte. All electrochemical measurements, cyclic voltammetry (CV), galvanostatic cycling with potential limitation (GCPL), and electrochemical impedance spectroscopy (EIS) were performed at room temperature using a computer-controlled multi-channel Potentiostat/Galvanostat Bio-Logic VMP3 work station driven by EC-Lab® v10.40 software with Z-fit tool for EIS data analysis. EIS measurements were carried out in the frequency ranging from 10 kHz to 10 mHz at the open circuit voltage, with AC voltage amplitude of 1.5 mV.

The specific capacitance (C_{sp}), maximum specific power density (P_{max}) and specific energy density (E_{sp}) were evaluated using the conventional eqn (1)–(5):[21,22]

$$C\ (\mathrm{F}) = \frac{i\Delta t}{\Delta V} \tag{1}$$

$$C_{sp}\ \left(\mathrm{F\ g^{-1}}\right) = \frac{4C}{m} \tag{2}$$

$$P_{max}\left(10^3\ \mathrm{W\ kg^{-1}}\right) = \frac{V^2}{4mR_{ir}}, \tag{3}$$

where

$$R_{ir}\ (\Omega) = \frac{\Delta V_{ir}}{2I} \tag{4}$$

$$E\left(\frac{1}{3.6}\ \mathrm{W\ h\ kg^{-2}}\right) = \frac{CV^2}{2m}, \tag{5}$$

where i (A) is the applied current, ΔV (V)/Δt (s) is the slope of the discharge curve, m (g) is the total mass of the two electrodes, C (F) is the calculated capacitance, V (V) is the maximum voltage obtained during charge, and R_{ir} is the internal resistance, which is determined from the voltage drop at the beginning of each discharge, whereas ΔV_{ir} represents the voltage drop.

Results and discussion

Material characterization

A one-pot hydrothermal route was used for the synthesis of MoS_2, CNS and MoS_2/CNS. Fig. 1 shows the SEM and TEM images of the CNS (Fig. 1c and d), confirming the spherical nature of the CNS in agreement with literature. The micrographs show the interconnected uniform amorphous CNS in the particle size diameter range of 100–200 nm. Fig. 1 compares the SEM and TEM images of the s-MoS_2 and s-MoS_2/CNS. The SEM and TEM micrographs of the s-MoS_2 (Fig. 1a and b) show the formation of a sphere-like morphology consisting of several agglomerated clusters of s-MoS_2 sheets.

A closer examination of the TEM images of the CNS (Fig. 1d) and s-MoS_2/CNS (Fig. 1f–h) clearly suggests a uniform dispersion and excellent integration of the MoS_2 with the CNS. The value of the *d*-spacing of the s-MoS_2 shown in the TEM image (Fig. 1i) is 0.62 nm, which is in agreement with literature.[23] In this synthesis method, it seems that the CNS particles acted as substrates for nucleation, wherein MoO_4^- ions reacted with sulphur ions from L-cysteine to form the MoS_2 sheets on the

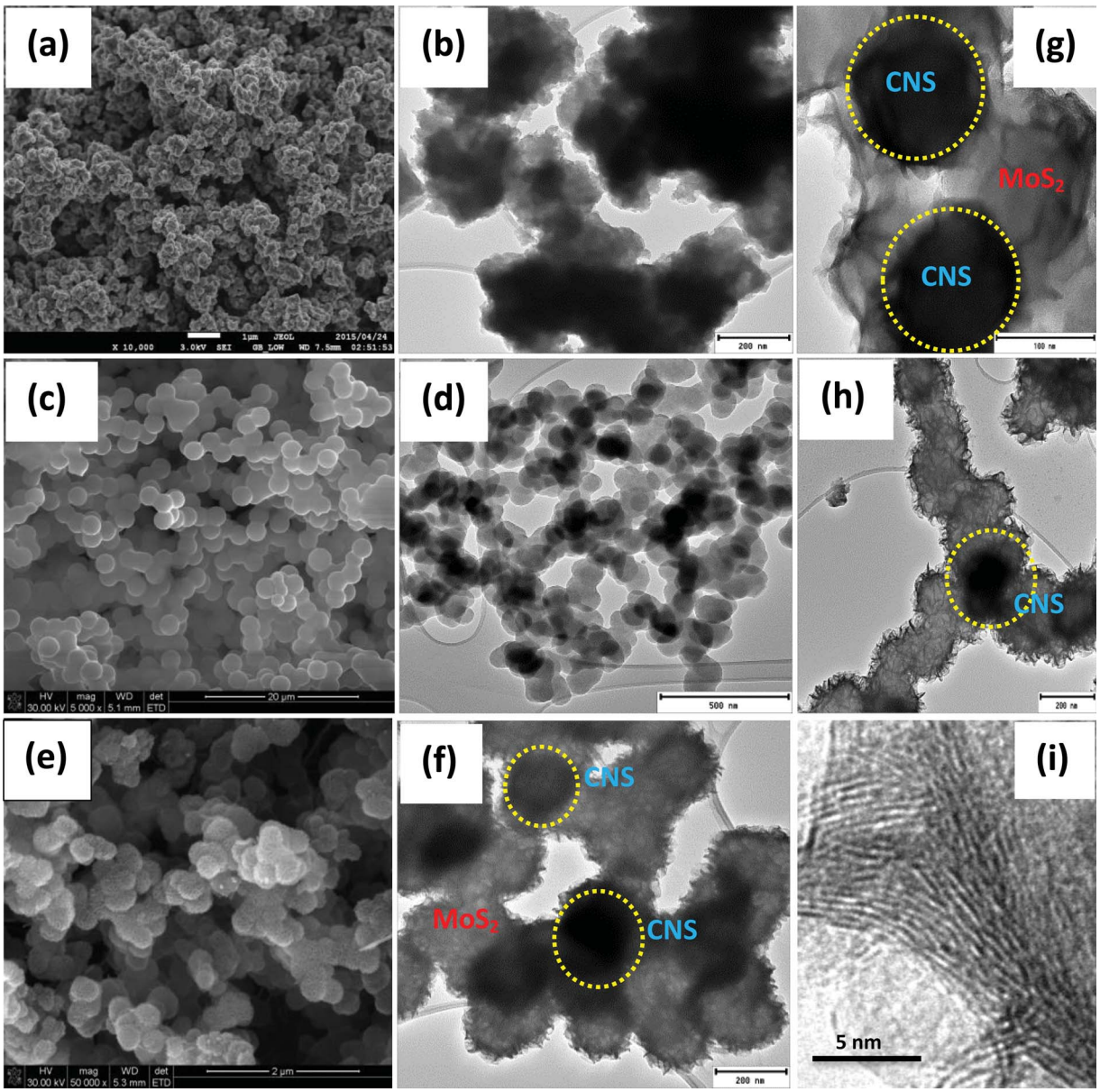

Fig. 1 SEM (a, c and e) and TEM (b, d, f, h and i) micrographs of s-MoS_2 (a and b), CNS (c and d), s-MoS_2/CNS (e and f); magnified views of s-MoS_2/CNS (g and h), and *d*-spacing of s-MoS_2 (i).

CNS. The presence of CNS prevented MoS_2 stacking and thus the formation of a porous 3-D sphere-like architecture with highly dispersed wrinkled and fluffy MoS_2 sheets on CNS particles. This unique structure is also apparent in the TEM images (Fig. 1f and h). In the s-MoS_2/CNS composite, the MoS_2 nano-sheet edges are readily exposed and not entangled as in MoS_2. This loose structure is desirable for superior charge storage. However, the MoS_2 sheets in the composite are not visible as layered; instead, they grew in various orientations and were intertwined around the spheres. An important consequence is the small accessible surface area coupled with the small micropores. This could potentially cause an obstruction for ion transportation and thus limit the capacitance. The elemental composition of as-synthesized s-MoS_2, obtained from the EDS (see ESI, Fig. S1†) obtained Na (3.35), S (66.11) and Mo (30.55) by weight percentage, clearly confirming the stoichiometry of the MoS_2. The impurity 'Na' is attributed to the starting precursor $Na_2MoO_4 \cdot 2H_2O$.

Similarly, the flower-like nanostructures (f-MoS_2) were obtained using a one-pot hydrothermal method. This method relies on sodium molybdate and thiourea to provide MoO_4^{2-} ions and sulphur atoms, respectively. Interestingly, the addition of small amounts of PEG in our synthesis protocol assisted in the efficient dispersion of the MoS_2 to generate the flower-like morphology. The starting precursor materials in the MoS_2 formation play a vital role, especially in the achieved morphology; a slight change, even in the reducing agent, can bring about enormous value. In this hydrothermal process, the

reaction involves three steps: (a) the hydrolysis of sulfur precursor to form H_2S, followed by (b) the reduction of Mo and (c) finally the formation of MoS_2.[19]

$$CS(NH_2)_2 + 2H_2O \rightarrow 2NH_3 + CO_2 + H_2S \quad (6)$$

$$4Na_2MoO_4 + 15CS(NH_2)_2 + 6H_2O \rightarrow 4MoS_2 + Na_2SO_4 + 6NaSCN + 24NH_2 + 9CO \quad (7)$$

The SEM and TEM images of as-synthesized MoS_2 in Fig. 2 clearly show flower-like hierarchical 3-D structures. The f-MoS_2 sheets self-assemble into a highly porous structure (Fig. 2a–c and e). The composite structure (Fig. 2d) also exhibits a clear flower-like morphology. The occurrence of this morphology may be associated with the presence of a surfactant (PEG-1000). Remarkably, after coating CNS with MoS_2 sheets, the surface appears rough and wrinkled by the MoS_2 sheets (Fig. 2d, f and g). The value of the *d*-spacing of the f-MoS_2 (Fig. 2h) is 0.61 nm, which is in agreement with literature.[23] The EDS data (see ESI, Fig. S2†) depict strong Mo and S overlapping signals, the MoS_2 contains Na 1.3 atomic%, S 62.09 atomic% and Mo 36.61 atomic%, confirming the stoichiometry of the MoS_2.

MoS_2 has a hexagonal crystal system and layer-structured D_{6h}^4 crystal system and $P6_3$ space group. Fig. 3 compares the XRD patterns of the CNS and its MoS_2 spherical and flower-like composites. There is no significant difference between the MoS_2 and MoS_2/CNS patterns, confirming good integration of the CNS with the MoS_2 structure. The diffraction peaks at 2θ = 15.8°, 37.9° and 41.5° are indexed to the hexagonal phase of MoS_2 (002), (100) and (201), respectively. For the spherical morphology (s-MoS_2/CNS composite), the diffraction peaks are similar to the individual s-MoS_2, meaning that CNS fully interacts with the MoS_2 and its presence does not interfere with the structure of the MoS_2. For the spherical material, s-MoS_2/CNS, the incorporation of CNS into the MoS_2 nanosheets decreases the intensity of the peaks, in particular the (002). The result indicates the formation of few layers of the MoS_2 in the composite; thus, CNS impedes the growth of the MoS_2 layer in a hexagonal array. Importantly, upon incorporation of the CNS, there is a slight shift in the diffraction lines of the MoS_2 to higher 2θ (see Fig. 3a–c), which is an indication of a lattice contraction. However, for the flower-like morphology (f-MoS_2/CNS), the incorporation of the CNS results in a slight shift to the lower 2θ (see Fig. 3d–f), which is an indication of lattice expansion in the S–Mo–S interlayer spacing and formation of a few layers of MoS_2. In addition, unlike the spherical composite (Fig. 3a–f), the presence of the CNS did not negatively impact the peak intensity of (002). In fact, the (002) peak became more intense and sharper, indicating a higher degree of crystallinity, comparable to that of the bulk MoS_2. This finding may be due to strong integration between the MoS_2 and CNS arising from the synthesis protocol adopted in this study, which allowed for the

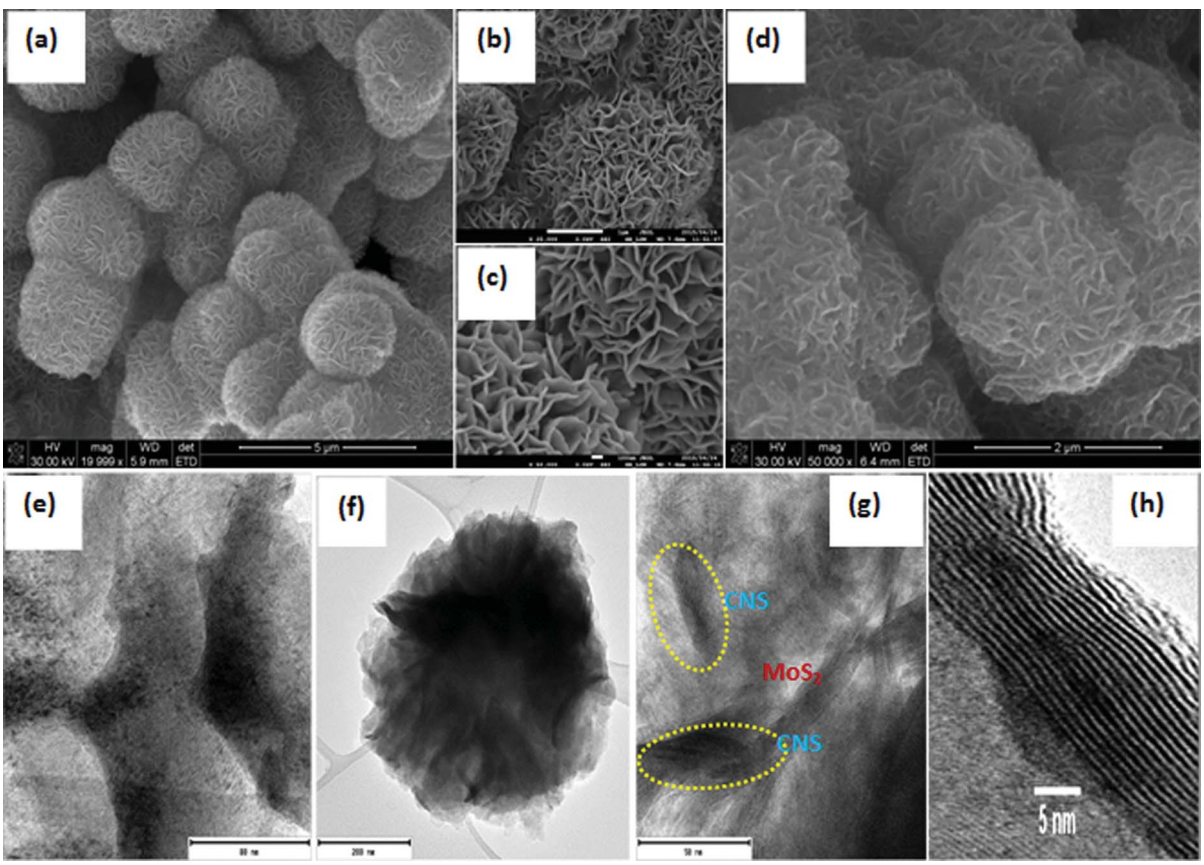

Fig. 2 SEM (a–d) and TEM (e–h) micrographs of f-MoS_2 (a–c), f-MoS_2/CNS (d), f-MoS_2 (e); magnified views of f-MoS_2/CNS (f and g) and *d*-spacing of f-MoS_2 (h).

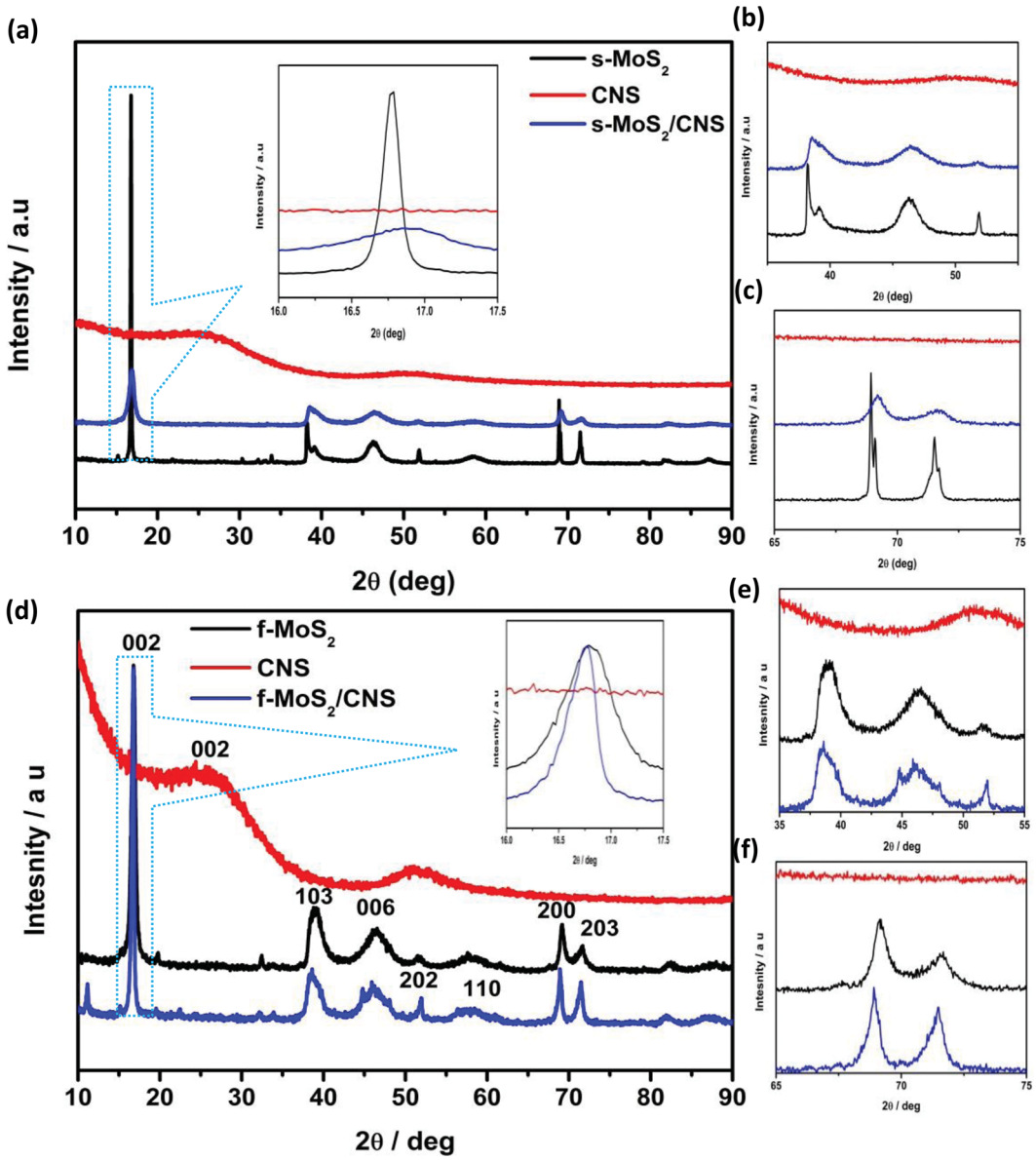

Fig. 3 XRD patterns of MoS_2, CNS and MoS_2/CNS composites for spherical (a–c) and flower-like (d–f) products and their magnified views.

two materials to undergo chemical reaction rather than just physical mixing. Furthermore, the peak (103) is more apparent, with a new broad peak (006) of hexagonal MoS_2 at 46° (Fig. 3d and e).

BET (five-point analysis) was used to measure the specific surface area and porosity of the as-synthesized materials. As shown in Table 1, the s-MoS_2 has a specific surface area of 17.8 $m^2\ g^{-1}$; on the other hand, the specific surface area of the s-MoS_2/CNS decreased to 9.17 $m^2\ g^{-1}$. This dramatic reduction is explained by the hindrance to the growth of the MoS_2, due to the presence of the CNS (also confirmed by the XRD patterns). In fact, the CNS makes the surface area of MoS_2 inaccessible. Moreover, the pore sizes of MoS_2 and MoS_2/CNS were revealed to be 22.9 and 18.61 nm, respectively. The f-MoS_2/CNS composite had a higher surface area with value of 61 $m^2\ g^{-1}$ compared to 25 $m^2\ g^{-1}$ recorded for the flower-like MoS_2. This means that incorporation of CNS prevented the agglomeration of MoS_2 sheets (also suggested from the XRD data). Surprisingly, the BET data follow the XRD data, especially the (002) peak height. Considering that capacitance is a function of the surface area, one would expect the materials with higher surface area (such as the f-MoS_2/CNS) to provide the best capacitance

Table 1 Porous texture of the as-synthesized materials

Sample	SA_{BET} ($m^2\ g^{-1}$)	Pore volume ($cm^3\ g^{-1}$)	Pore size (nm)
s-MoS_2	17.80	0.100	22.93
s-MoS_2/CNS	9.17	0.040	18.61
f-MoS_2	25.00	0.018	36.13
f-MoS_2/CNS	61.00	0.020	14.68

Table 2 Comparison of Raman spectral data

	Raman shift/cm^{-1}							
	s-MoS_2		s-MoS_2/CNS		f-MoS_2		f-MoS_2/CNS	
	E^1_{2g}	A_{1g}	E^1_{2g}	A_{1g}	E^1_{2g}	A_{1g}	E^1_{2g}	A_{1g}
Peak position	375.69	402.49	375.07	400.84	374.91	401.78	375.23	400.95
$\lvert E^1_{2g} - A_{1g}\rvert$	26.8		25.77		26.87		25.72	
FWHM	8.47	8.23	8.19	8.71	9.29	8.72	13.55	10.88

value. Moreover, despite the fact that the pores do not directly contribute to the surface area, they provide accessible pathways for easy diffusion of ions and reversible charge storage.

Raman spectroscopy was used to provide more insight into the structure and topology of the as-synthesized MoS_2-based nanocomposites. Fig. 4 shows the Raman spectra of as-synthesized MoS_2 nanosheets, CNS and MoS_2/CNS nanocomposites. The CNS exhibited the signature D and G peaks of carbon-based materials at 1347 and 1590 cm^{-1}, respectively. As we expected, the MoS_2/CNS composites also showed the D and G peaks close to the regions wherein they were observed for the CNS alone, confirming the successful integration of the CNS into the two MoS_2-based composites. There was no detectable difference in the intensity ratios of the D to G band ($I_D : I_G$) of the CNS (0.95), s-MoS_2/CNS (0.94) and f-MoS_2/CNS (0.94), which implies that the CNS essentially retained its pristine structure even after integration with the MoS_2. The characteristic Raman bands for bulk s-MoS_2 were observed at 375.69 and 402.49 cm^{-1} due to E^1_{2g} and A_{1g} modes with full-widths at half maximum (FWHM) of 8.47 and 8.23 cm^{-1}, respectively. The E^1_{2g} mode describes the in-layer displacement of the Mo and S atoms, whereas the A_{1g} mode relates to the out-of-layer symmetric displacements of S atoms along the *c* axis.[24,25] Interestingly, the incorporation of the CNS into the MoS_2 resulted in the slight softening of these two Raman bands compared to those of the bulk MoS_2; the spherical MoS_2/CNS appeared at 375.07 cm^{-1} (E^1_{2g}) and 400.84 cm^{-1}

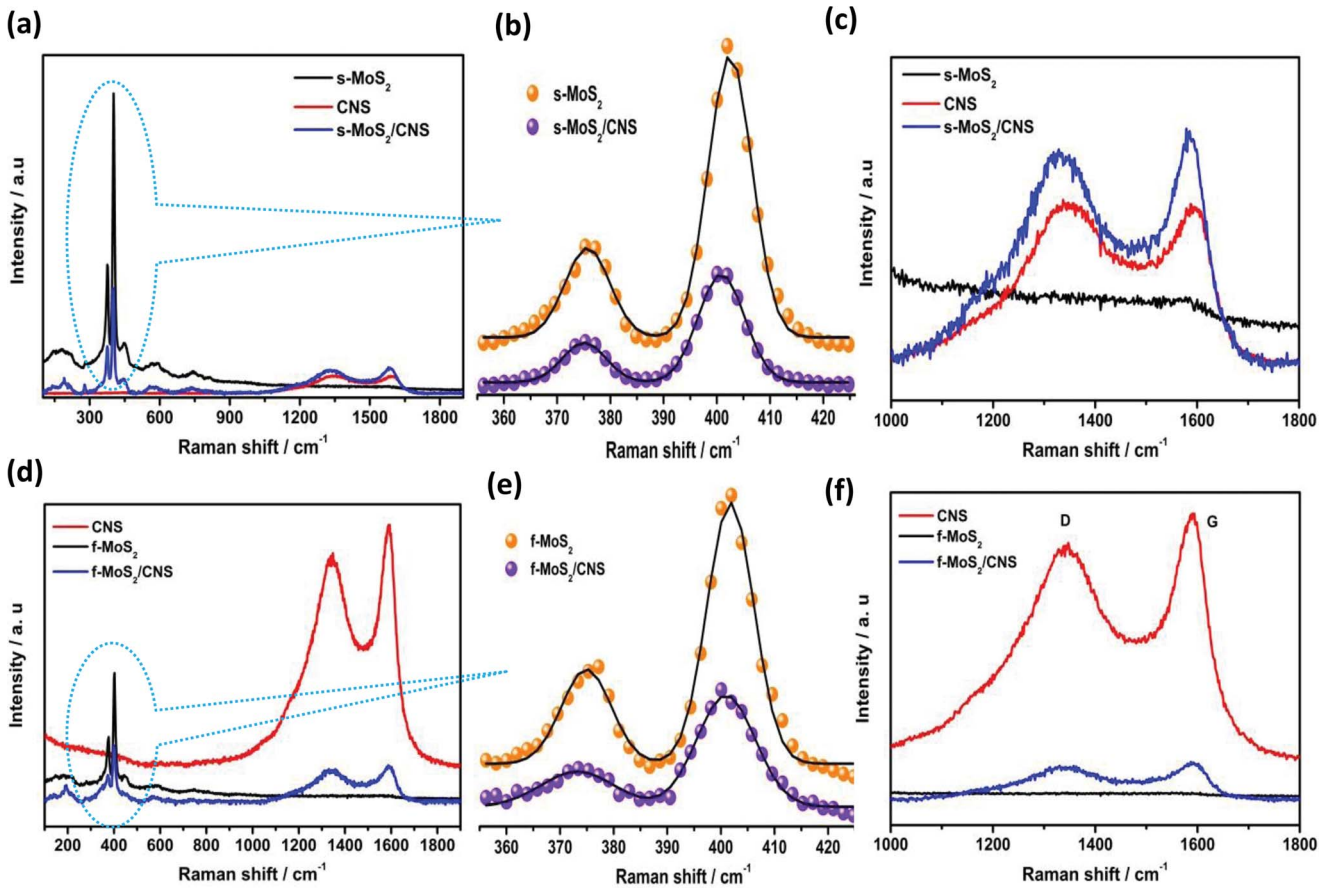

Fig. 4 Raman spectra of spherical (a–c) and flower-like (d–f) MoS_2, CNS and MoS_2/CNS nanocomposites and their magnified views.

(A_{1g}), while the flower-like morphology appeared at 374.91 cm^{-1} (E^1_{2g}) and 401.78 cm^{-1} (A_{1g}). Moreover, the increase in the FWHM values were more pronounced for the flower-like morphology than for the spherical morphology.

In the flower-like morphology, FWHM values are larger in the f-MoS_2/CNS than in the bulk f-MoS_2 (*cf.* $E^1_{2g} = 13.55$ *vs.* 9.29 cm^{-1} of the bulk f-MoS_2 or $A_{1g} = 10.88$ *vs.* 8.72 cm^{-1} of the bulk f-MoS_2). The broadening of the Raman bands is related to phonon confinement and also indicates that the lateral dimensions of these MoS_2 layers are in the nano-dimension.[25] The larger FWHM for the f-MoS_2/CNS compared to its s-MoS_2/CNS counterpart is indicative of the smaller particle sizes and larger surface area, which corroborates the BET analysis. In a recent study by Lee *et al.*,[26] the authors showed that the frequency difference between E^1_{2g} and A_{1g} modes could serve as a convenient and robust diagnosis of the layer thickness of MoS_2 samples. From our results in Table 2, the frequency difference (*i.e.*, $|E^1_{2g} - A_{1g}|$) decreases as follows: bulk MoS_2 (*ca.* 27 cm^{-1}) > f-MoS_2/CNS (*ca.* 26 cm^{-1}) = s-MoS_2/CNS (*ca.* 26 cm^{-1}). Thus, our results indicate that there is no significant difference in the layer thicknesses of the two MoS_2/CNS composites and the two synthesis methods we adopted in this study further confirm the change in the physicochemical properties of the MoS_2 complexes.

Fig. 5 shows FT-IR spectra of the MoS_2, CNS and MoS_2/CNS nanocomposites. In MoS_2, the peaks at 1583 and 1518 cm^{-1} are consistent with NH_2 in-group deformation (arising from the thiourea or L-cysteine used in the synthesis), and the peak at 1466 cm^{-1} is assigned to the N–C–N asymmetric stretching mode. The band at 1231 cm^{-1} is assigned to stretching vibrations of O–H bonds. The C–O–H stretching mode occurred at 1092 cm^{-1}. The C–S stretching vibrations are observed at 729 cm^{-1}. The weak peak around 600 cm^{-1} is assigned to Mo–S vibration. Similar peaks are observed for the MoS_2/CNS nanocomposite with the additional peaks at 2892 cm^{-1} and 2971 cm^{-1} due to C=C symmetric and asymmetric stretching vibrations as explained elsewhere.[27] Indeed, the presence of the functional groups on the CNS could have contributed to the efficient integration of the CNS with the MoS_2 (as observed in the TEM images).

Fig. 6 compares the XPS data of s-MoS_2/CNS (Fig. 6a and b) and f-MoS_2/CNS (Fig. 6c and d). XPS analysis reveals the predominant Mo 3d and S 2p characteristic peaks for both s-MoS_2/CNS and f-MoS_2/CNS. The two materials clearly show that the only elements present are Mo, S, adventitious C and O, and Na 'impurity' (Table 3).

Both materials show the typical spectral signature of MoS_2, with the co-existence of metallic (1T) and semiconducting (2H) phases.[28–30] There is a clear difference between the two complexes, notably the S 2p splits into two peaks in the s-MoS_2/CNS (162.42 and 163.67 eV for S $2p_{3/2}$ and S $2p_{1/2}$, respectively), whereas the f-MoS_2/CNS splits into four peaks (located at 162.31, 163.34, 164.63 and 169.23, which are assigned to S $2p_{3/2}$, S $2p_{1/2}$, S_2^{2-} or S^{2-} and S^{4+}, respectively), suggesting that the S atoms exist in two different chemical states. This finding is indicative of f-MoS_2/CNS undergoing partial oxidation into MoS_xO_y at the edges and defect sites, which effectively leads to

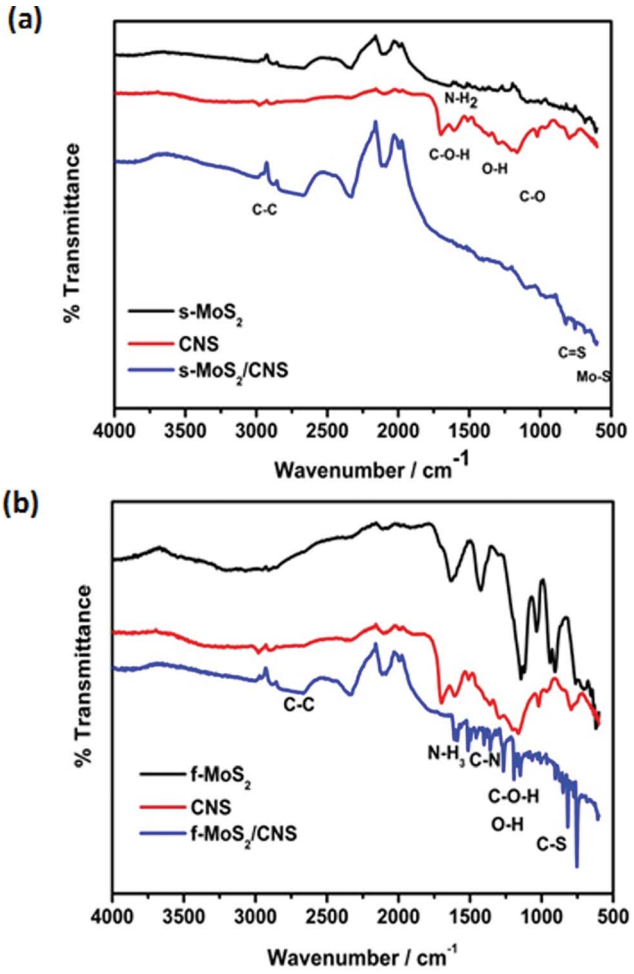

Fig. 5 FT-IR spectra of spherical (a) and flower-like (b) MoS_2, CNS and MoS_2/CNS nanocomposites.

enhanced redox processes. The molybdenum spectra (Fig. 6a and c) show the expected Mo $3d_{5/2}$ and Mo $3d_{3/2}$, including the Mo^{6+} species (*ca.* 236 eV) usually observed in partially oxidized MoS_2 complexes. In addition to the significant changes in the S 2p of the f-MoS_2/CNS, its surface atoms, with the exception of O and Na, are lower than observed for the s-MoS_2/CNS. Considering that surface Na species are involved in the storage mechanism, one may conclude that Na will be more accessible to the f-MoS_2/CNS in an aqueous solution for enhanced energy storage than the s-MoS_2/CNS.

Electrochemical properties

Fig. 7a shows the cyclic voltammetric (CV) evolutions of the individual CNS, s-MoS_2 and f-MoS_2 obtained from the 3-electrode configuration in 1 M Na_2SO_4 at 5 mV s^{-1}. These results show that s-MoS_2 is more capacitive than the f-MoS_2 but, as it will be shown later, the capacitance retention of the s-MoS_2 is worse than that of the f-MoS_2. From Fig. 7a, it is evident that CNS do not show any significant current response. Fig. 7b compares the CVs of the composite materials, showing that the f-MoS_2/CNS has better performance (high current response and

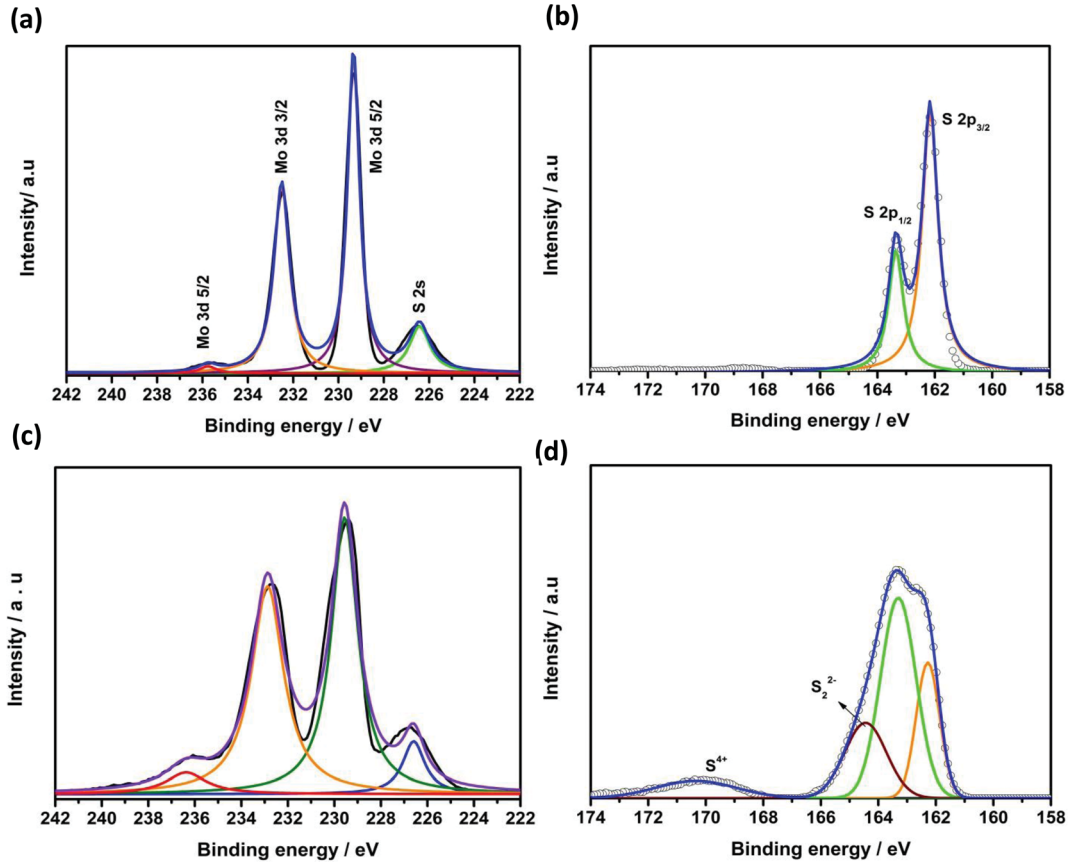

Fig. 6 High resolution XPS analysis of s-MoS_2/CNS (a and b) and f-MoS_2/CNS (c and d). Mo 3d (a and c) and S 2p (b and d).

Table 3 XPS data for the s-MoS_2/CNS and f-MoS_2/CNS samples

	Binding energy/eV			Atomic/%, det. limit of 0.1 at%				
Sample	Mo $3d_{5/2}$	Mo $3d_{3/2}$	Mo $3d_{5/2}$	Mo 3d	S 2p	C 1s	O 1s	Na
s-MoS_2/CNS	229.33	232.70	235.75	25.5	31.6	29.8	12.1	1.0
f-MoS_2/CNS	229.00	232.80	236.50	22.8	28.4	15.8	23.1	9.9

slightly wider voltage window) compared to the s-MoS_2/CNS. Fig. 7c and d exemplify typical GCPL curves of the various symmetric cells obtained in 1 M Na_2SO_4 at 0.5 A g^{-1}. The performance of the s-MoS_2 is better than its composite, whereas the f-MoS_2/CNS is better than its precursor f-MoS_2. As will be shown later, the nanocomposite materials (both spherical and flower-like) show better capacitance retention and cycling stability than their MoS_2 materials. As observed in Fig. 7, the CV and GCPL curves of the composite materials, notably the flower-like materials, show quasi-rectangular shapes, which is a strong deviation from the ideal rectangular shape that was expected from the EDLC. Furthermore, the GCPL of the flower-like composite (Fig. 7d) shows a broad peak at around 0.3 V. These results clearly confirm the pseudocapacitive behavior of these MoS_2-based composite materials.

Fig. 8 shows the plots of specific capacitance *versus* current densities. With the exception of the s-MoS_2/CNS-based cell, the capacitance values of all the cells decrease with increasing gravimetric currents. The capacitance of the s-MoS_2/CNS-based cell remains essentially the same (*cf.* 108 F g^{-1} at 0.1 A g^{-1} *versus* 94 F g^{-1} at 1 A g^{-1}, which is about 13% capacitance loss). This ability of the s-MoS_2/CNS to maintain high capacitance even at high current density is indicative of high-power performance.

Table 4 compares the values of capacitance, maximum energy and power density of the symmetric cells; unfortunately, there is no related literature with which to compare our results, except for 3-electrode systems. The maximum specific capacitance for the flower-like composite f-MoS_2/CNS electrodes is 231 F g^{-1}, with maximum energy density 26 W h kg^{-1} and power density 6443 W kg^{-1}. For the sphere-like morphologies, the equivalent values obtained were 108 F g^{-1}, 7.4 W h kg^{-1} and 3700 W kg^{-1}. The inferior performance of the s-MoS_2/CNS electrodes can be explained by the inaccessible surface area for charge storage in the MoS_2/CNS composite due to the presence

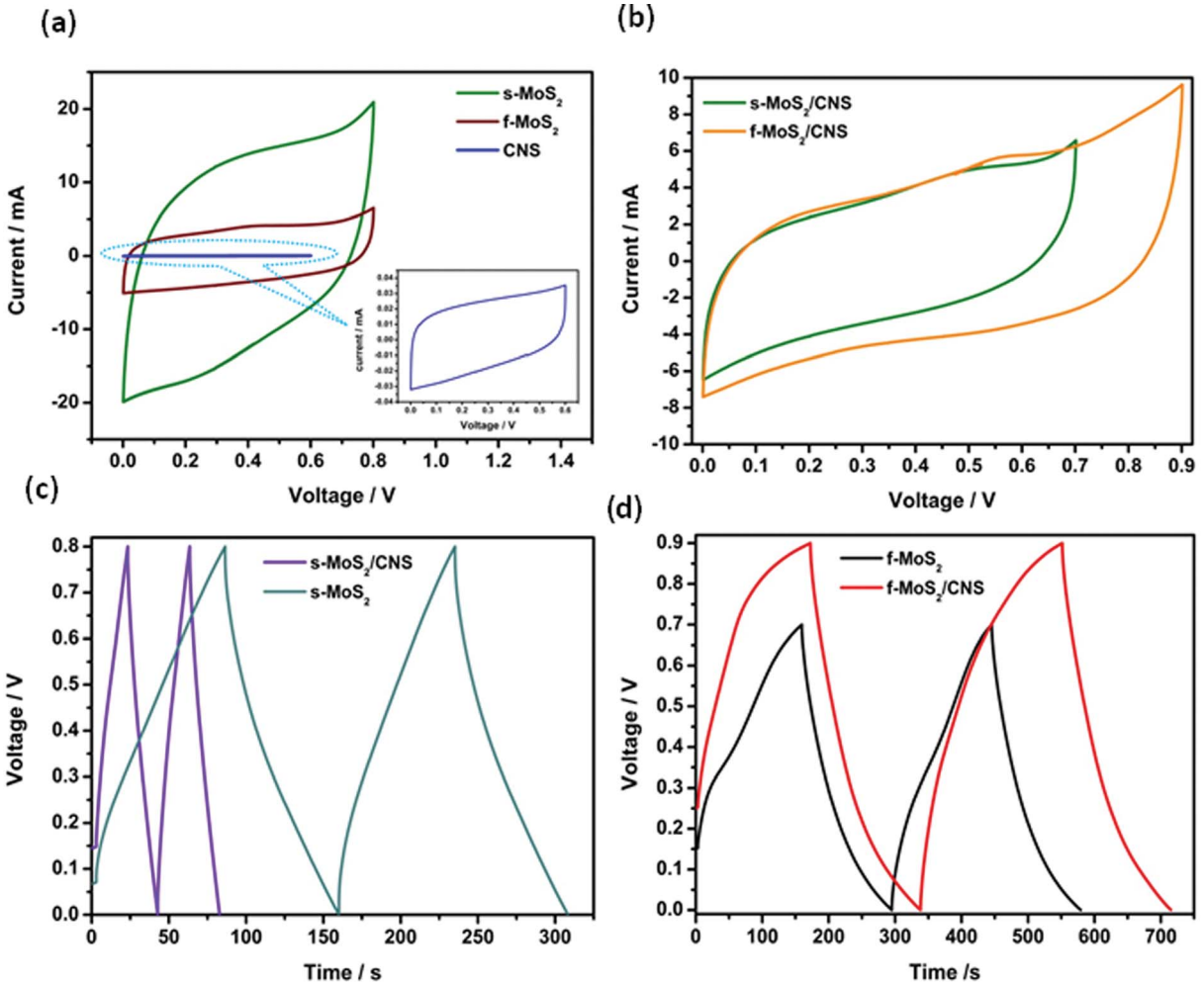

Fig. 7 CV comparison of (a) s-MoS_2, f-MoS_2 and CNS; (b) s-MoS_2/CNS and f-MoS_2/CNS. GCPL comparison of (c) s-MoS_2/CNS and s-MoS_2, and (d) f-MoS_2/CNS and f-MoS_2. Conditions: CVs obtained at 5 mV s^{-1}, while the GCPL was obtained at 0.5 A g^{-1}; all data were acquired in 1 M Na_2SO_4.

of CNS, as shown by the Raman spectroscopic data. The maximum energy density achievable with f-MoS_2/CNS (26 W h kg^{-1}) is more than twice that of MoS_2 (10 W h kg^{-1}) alone. The high energy density is owed to the favorable porous nanostructure of the composite, in which MoS_2 sheets serve as active sites for redox reactions, coupled with CNS interaction with electrolyte and the synergistic effects of MoS_2/CNS composites.

In theory, the specific capacitance of the MoS_2 may be estimated from the amount of power needed to carry out the electrolysis of 1 mol of active material (*i.e.*, 1 F = 96 485 C) and the molar mass of the material (MoS_2 = 160.07 g mol^{-1}) using the eqn (8):[31]

$$F = \frac{Q}{U} \tag{8}$$

where U is the voltage window and Q is electrical energy per 1 gram. Because our U ranges between 0.8 and 1 V, the theoretical pseudocapacitance is between 603 and 754 F g^{-1}. If we consider that the supercapacitance of a 3-electrode cell is about a quarter that of a 2-electrode system, our value for the f-MoS_2/CNS based symmetric pseudocapacitor (231 F g^{-1}) is in good agreement with theory.

Voltage-holding cycling experiments, complemented with EIS experiments, were performed to provide insight into the cycling stability of the four symmetric cells. The zeroth hour cycling capacitance (brown data points in Fig. 9 and 10) for each of the four symmetric cells was found to be lower than that at the 10th hour cycling, which suggests that MoS_2-based cells require a significant amount of time to equilibrate prior to recording data from voltage-holding tests. Thus, the best voltage-holding test data were obtained from the 10th hour. Fig. 9 exemplifies the typical voltage-holding test performed at 0.7 A g^{-1} for the spherical morphology. At the 10th hour, the s-MoS_2 started with about 140 F g^{-1} and obtained 20 F g^{-1} at the end of the 50th hour (Fig. 9a), which is about 86% loss of capacitance. The composite s-MoS_2/CNS started with about 90 F g^{-1}, but maintained 55 F g^{-1} at the end of the 50th hour (Fig. 9c), which is about 39% loss of capacitance. The fitted EIS data for both the s-MoS_2 (Fig. 9b) and its composite form (s-MoS_2/CNS, Fig. 9d) obtained before and after the 50 hour long-cycling

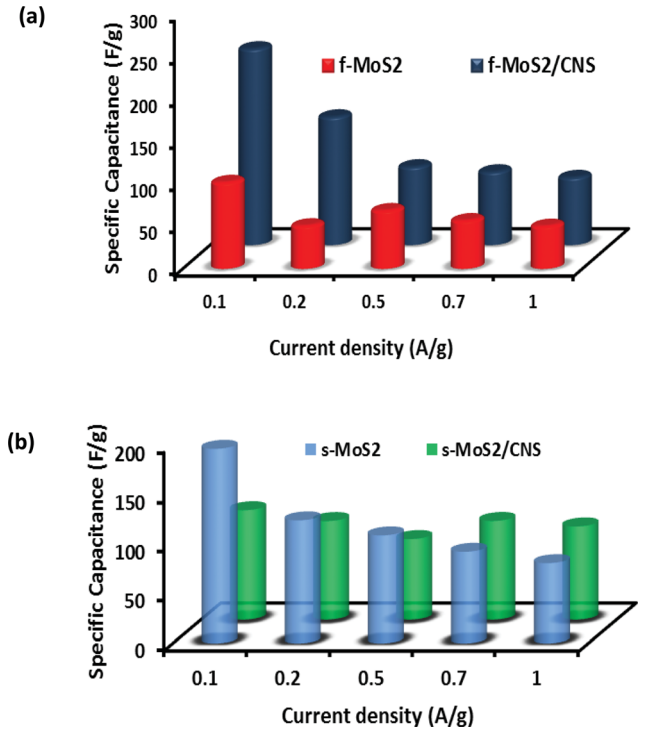

Fig. 8 GCPL results for specific capacitance at various current densities of spherical and flower-like MoS_2 and MoS_2/CNS.

experiments are summarized in Table 5. For the flower-like materials (Fig. 10), the capacitance of the f-MoS_2 at the 10th hour was about 24 F g^{-1} and obtained 14 F g^{-1} at the end of the 50th hour (Fig. 10a), which is about 42% loss of capacitance. The composite f-MoS_2/CNS started with about 90 F g^{-1}, but maintained 84 F g^{-1} at the end of the 50th hour (Fig. 10c), which is a mere 6% loss of capacity. The fitted EIS data for both the f-MoS_2 (Fig. 10b) and its composite form (f-MoS_2/CNS, Fig. 10d), obtained before and after the 50 hour long-cycling experiments are summarized in Table 6.

From the results of the cycling performances of the spherical (Fig. 9) and flower-like (Fig. 10) materials, the following important findings should be emphasized. First, the zeroth hour cycling capacitance for each of the cells was found to be lower than that at the 10th hour cycling, which suggests that MoS_2-based cells or related layered materials require a significant amount of time to equilibrate prior to recording data from voltage-holding tests. Second, the cycling stability for MoS_2 is very poor, but can be greatly improved by integrating it with conductive carbon materials such as the CNS. Third, the cycling stability of the cells from the MoS_2 or its carbon composite is strictly dependent on its morphology; the flower-like morphology shows enhanced electrochemistry compared to the spherical morphology.

Finally, to obtain some insight into the capacitive properties of the cells, we were able to satisfactorily fit the raw EIS data with the electrical equivalent circuit (EEC). The EEC consists of Voigt RC elements (Fig. 9e), involving series resistance (R_s), charge-transfer resistance (R_{ct}) and constant-phase elements (CPE or Q). For the cell with the spherical morphology (Table 5), the R_s values of the s-MoS_2 before and after the 50th hour were 0.23 and 0.49 Ω, respectively. For the s-MoS_2/CNS, the R_s values before and after the 50th hour were 0.33 and 1.14 Ω, respectively. The combined R_{ct} values before and after the 50th hour were 16.26 and 17.28 Ω, respectively. For the s-MoS_2/CNS it was 2.45 Ω before and 4.62 Ω after the 50th hour cycling. The result clearly proves that the presence of the CNS enhanced the conductivity of the s-MoS_2-based cells. However, the data for the cells fabricated from the flower-like morphology (Table 6), the R_s values of the f-MoS_2 before and after the 50th hour, were 0.21 and 0.40 Ω, respectively. For the f-MoS_2/CNS, the R_s values before and after the 50th hour were 0.26 and 0.31 Ω, respectively. The combined R_{ct} values for the f-MoS_2 before and after the 50th hour were 3.43 and 4.14 Ω, respectively. For the f-MoS_2/CNS, it was 3.37 before and 5.09 Ω after the 50th hour cycling. Like the s-MoS_2-based cells, the results for the f-MoS_2-based cells suggest that the CNS component serves to decrease the internal resistance of the f-MoS_2, thereby improving the conductivity and

Table 4 Comparison of the capacitive performance of various MoS_2-based supercapacitors[a]

Aqueous electrolyte	Electrode material	Device configuration	Voltage (V)	C_{sp}/ F g^{-1}	E_{sp}/ W h kg^{-1}	P_{max}/ W kg^{-1}	Ref.
1 M Na_2SO_4	f-MoS_2/CNS	Symmetric	0.9	231	26	6443	This work
1 M Na_2SO_4	s-MoS_2/CNS	Symmetric	0.7	108	7.4	3700	This work
1 M Na_2SO_4	s-MoS_2	Symmetric	1.0	195	27	8750	This work
1 M Na_2SO_4	f-MoS_2	Symmetric	0.8	96	8.59	4000	This work
1 M Na_2SO_4	MoS_2	3-Electrode	0.7	92.85	7.25	186.5	14
1 M H_2SO_4	PANI/MoS_2	3-Electrode	1.0	575	265	18 000	2
1 M KCl	PPy/MoS_2	3-Electrode	0.8	553.7	49	400	8
1 M Na_2SO_4	MoS_2–graphene composite	3-Electrode	1.0	243	85	7600	6
1 M Na_2SO_4	MoS_2/RGO	3-Electrode	0.6	253	12.65	300	10
1 M Na_2SO_4	MoS_2/MWCNT	3-Electrode	1.0	452.7	—	—	12
3 M KOH	Porous tubular C/MoS_2	3-Electrode	0.5	210	—	—	14

[a] Key: PANI = polyamine; PPy = polypyrrole; RGO = reduced graphene oxide; MWCNT = multi-walled carbon nanotubes.

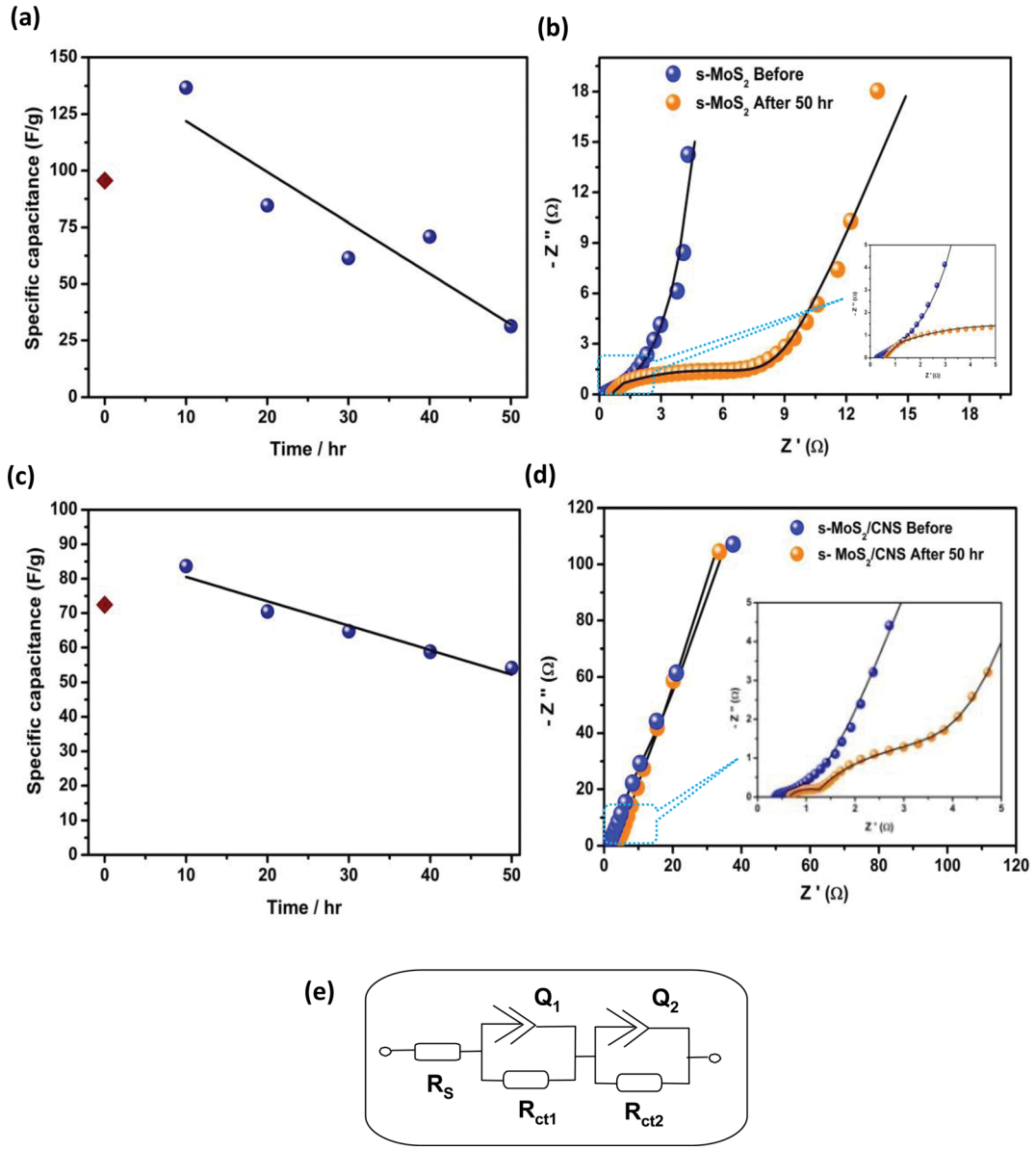

Fig. 9 Typical GCPL plots at 0.7 A g^{-1} (a and c) and Nyquist plots (b and d) obtained before and after 50 hour voltage experiments for the spherical (a and b) MoS_2 and MoS_2/CNS-based (c and d) symmetric pseudocapacitors. The electrical equivalent circuit used in fitting the Nyquist plots is shown in (e).

capacitance of the f-MoS_2/CNS-based symmetric pseudocapacitor. The impedance of the CPE (Z_{CPE}) is related to the frequency-independent constant (Q) and radial frequency (w) according to the eqn (9):[32]

$$Z_{CPE} = \frac{1}{[Q(jw)^n]} \quad (9)$$

where n (with values in the $-1 \leq n \leq 1$ range) is obtained from the slope of log Z *versus* log f. When $n = 0$, 1, -1 or 0.5, the CPE describes a pure resistor, a pure capacitor, an inductor, or Warburg impedance (Z_w), respectively, due to the diffusion of the ions. For all the cells, the n values observed for these electrodes are generally greater than 0.5, which confirms the pseudocapacitive properties of the MoS_2-based symmetric cells, corroborating the CV data in Fig. 7a and b.

The data for the Bode plots (see ESI, Fig. S3†) summarised in Tables 5 and 6 show that the phase angle for each of the systems before and after 50 hour cycling was greater than $-75°$, but lower than the $-90°$ expected of an ideal EDLC system. The phase angle result is a further confirmation of the pseudocapacitive behaviour of these MoS_2-based systems. In addition, the knee frequency (f_o, $\phi = 45°$), which is the maximum frequency at which the dominant behaviour of the supercapacitor (power density), can be observed. The knee frequency relates to the rate or power capability of the supercapacitor; the higher the f_o value is, the more rapidly such a supercapacitor can be charged and discharged. The f_o values for the s-MoS_2/CNS are 50 Hz (time constant = 0.02 s) before cycling and 5 Hz (time constant = 0.2 s) after the 50th hour voltage-holding testing. However, for the f-MoS_2/CNS system, the f_o value

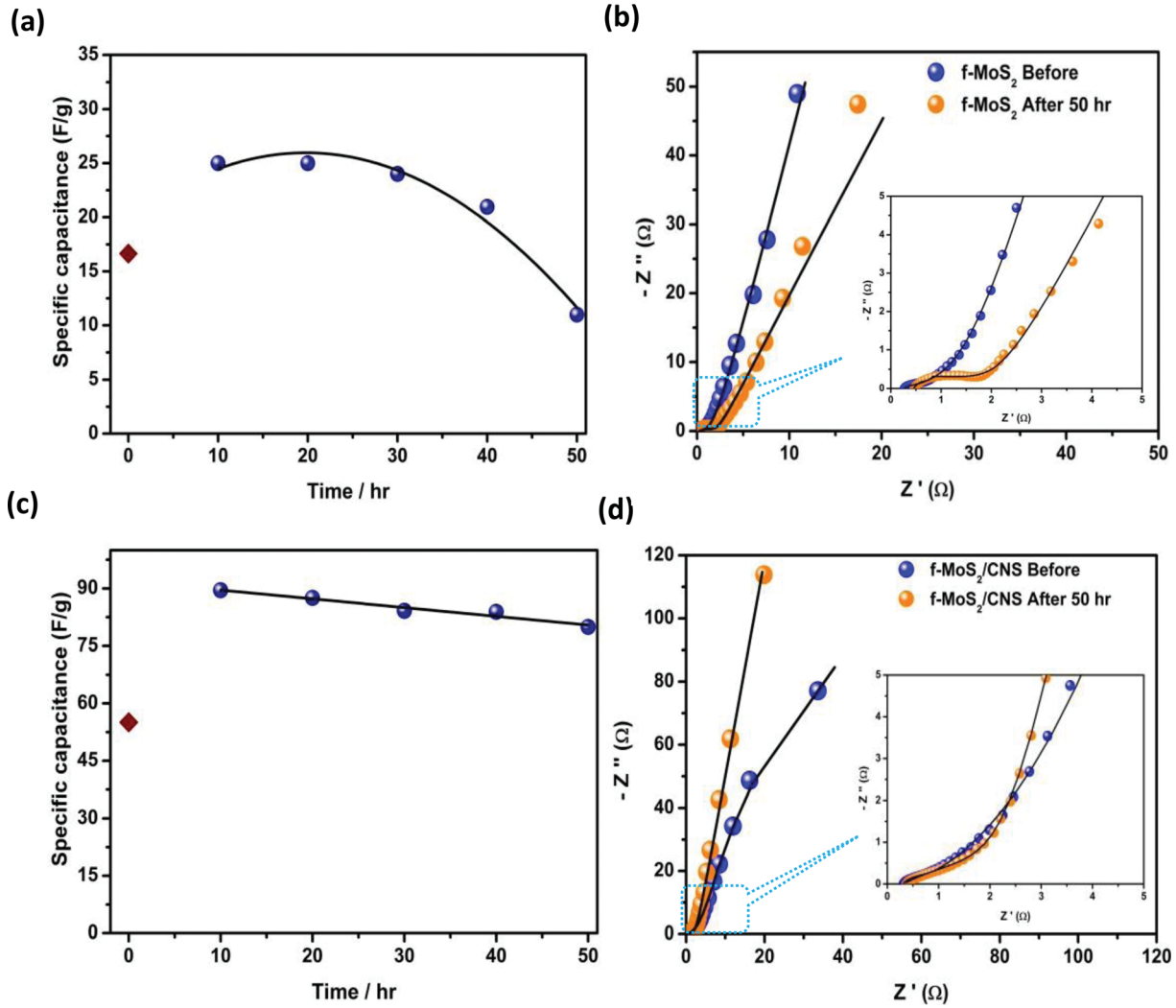

Fig. 10 Typical GCPL plots at 1 A g^{-1} for f-MoS_2 (a) and 1.5 A g^{-1} for f-MoS_2/CNS (c); Nyquist plots for f-MoS_2 (b) and f-MoS_2/CNS (d) obtained before and after 50 hour voltage experiments. The electrical equivalent circuit used in fitting the Nyquist plots is shown in Fig. 9e.

Table 5 Cycling performance of the spherical MoS_2 and MoS_2/CNS based symmetric pseudocapacitors in 1 M Na_2SO_4. EIS data before and after 50 h voltage-holding experiments were fitted with the Voigt equivalent circuit

	s-MoS_2//s-MoS_2		s-MoS_2/CNS//s-MoS_2/CNS	
Parameter	0^{th} hour cycle	50^{th} hour cycle	0^{th} hour cycle	50^{th} hour cycle
R_s/Ω	0.23 ± 0.05	0.49 ± 0.06	0.33 ± 0.19	1.14 ± 0.87
Q_1/mF s$(\alpha - 1)$	0.33 ± 0.08	0.47 ± 0.03	0.2 ± 0.03	2.21 ± 0.11
n_1	0.40 ± 0.09	0.77 ± 0.15	0.82 ± 0.17	0.64 ± 0.18
R_{ct1}/Ω	3.75 ± 0.42	10.08 ± 2.7	0.72 ± 0.21	1.39 ± 0.13
Q_2/mF s$(\alpha - 1)$	8.10 ± 0.34	8.70 ± 0.02	13.32 ± 1.32	9.38 ± 0.02
n_2	0.80 ± 0.25	0.80 ± 0.22	0.47 ± 0.29	0.83 ± 0.17
R_{ct2}/Ω	12.51 ± 0.07	7.20 ± 1.95	1.73 ± 0.55	3.23 ± 0.29
Phase angle	−73°	−53°	−80°	−80°
Knee frequency	1 Hz	1 Hz	50 Hz	5 Hz

remained at 50 Hz before and after the voltage-holding test, which is a further confirmation of the high electrochemical cycling stability of the f-MoS_2/CNS system.

The energy-storage mechanism of MoS_2 in aqueous supercapacitors is well described in the literature;[29,31] it is the combined phenomena involving the transition from EDLC to

Table 6 Cycling performance of the flower-like MoS_2 and MoS_2/CNS based symmetric pseudocapacitors in 1 M Na_2SO_4. EIS data before and after 50 h voltage-holding experiments were fitted with the Voigt equivalent circuit

	f-MoS_2//f-MoS_2		f-MoS_2/CNS//f-MoS_2/CNS	
Parameter	0^{th} hour cycle	50^{th} hour cycle	0^{th} hour cycle	50^{th} hour cycle
R_s/Ω	0.21 ± 0.102	0.4 ± 0.1	0.26 ± 0.08	0.31 ± 0.17
Q_1/mF s$(\alpha - 1)$	0.2 ± 0.14	0.16 ± 0.03	0.12 ± 0.07	0.17 ± 0.02
n_1	0.67 ± 0.19	0.73 ± 0.1	0.84 ± 0.14	0.90 ± 0.13
R_{ct1}/Ω	1.70 ± 0.62	1.57 ± 0.16	0.32 ± 0.13	1.28 ± 0.74
Q_2/mF s$(\alpha - 1)$	21.12 ± 0.07	9.4 ± 0.08	12.24 ± 0.68	9.64 ± 0.36
n_2	0.85 ± 0.15	0.62 ± 0.13	0.68 ± 0.21	0.47 ± 0.29
R_{ct2}/Ω	1.73 ± 0.18	2.57 ± 1.24	3.05 ± 0.18	3.81 ± 0.41
Phase angle	−78°	−70°	−75°	−80°
Knee frequency	10 Hz	10 Hz	50 Hz	50 Hz

the pseudocapacitive process (faradaic/redox process) and increased active surface area due to possible exfoliation. First, there is the accumulation of ions at the double layer interface between the MoS_2 flakes and the electrolyte. This is subsequently accompanied by a redox process: upon charging (reduction), the alkali metal ions in the electrolyte (Na^+) adsorb onto the surface and intercalate between the MoS_2 layers, followed by deintercalation upon discharging (oxidation), as shown in eqn (10).

$$MoS_2 + Na^+ + e^- \rightleftarrows MoS\text{–}SNa \quad (10)$$

The repeating intercalation–deintercalation process of the sodium ions over several cycles leads to partial exfoliation of the MoS_2 layers, resulting in an increased surface area and enhanced specific capacitance. The evidence for the possible partial exfoliation of the MoS_2 during the repeated intercalation–deintercalation process of electrolyte ions can be observed from the zeroth hour cycling capacitance (brown data points in Fig. 9 and 10 described above), which was lower than the 10^{th} hour cycling before stabilizing.

Conclusions

Two variants of carbon nanosphere-modified molybdenum disulphide (MoS_2/CNS) nanostructures were successfully synthesized by a simple one-pot hydrothermal method. The two different synthetic methods obtained two different morphologies: flower-like (f-MoS_2/CNS) and spherical (s-MoS_2/CNS) morphologies. The physical and chemical characterisations reveal that the two materials were properly integrated into the CNS surface. The addition of CNS impedes the growth of the s-MoS_2 crystals in the composite, but enhances the growth of the f-MoS_2, particularly in the (002) plane of hexagonal MoS_2. The f-MoS_2/CNS shows lattice expansion and large surface area, whereas the s-MoS_2/CNS shows lattice contraction and smaller surface area. The presence of CNS on the MoS_2 structure leads to slight softening of the characteristic Raman bands (E^1_{2g} and A_{1g} modes) with larger FWHM. The electrochemical capacitive behaviour of the MoS_2-based materials was evaluated in symmetric cells. The electrochemical performance of the composites demonstrates that the MoS_2/CNS composite from flower-like MoS_2 exhibits better capacitance, energy and power densities (231 F g^{-1}, 26 W h kg^{-1} and 6443 W kg^{-1}) compared to the spherical morphology (108 F g^{-1}, 7.4 W h kg^{-1} and 3700 W kg^{-1}). CNS play a vital role in improving the electrochemical properties of the MoS_2-based electrode materials, especially with respect to improving the capacitance retention (*i.e.*, stable electrochemical cycling). The excellent electrochemical performance of MoS_2/CNS was accredited to the morphology of the composite and synergistic effects between MoS_2 sheets and CNS. These findings show great promise for future studies of MoS_2 modified with other conducting carbon nanostructures for the development of high-performance electrochemical energy storage systems.

Acknowledgements

This study was supported by the University of the Witwatersrand (Wits) and CSIR, South Africa. The support of the Wits Materials for Energy Research Group (MERG) towards this research is gratefully acknowledged. Opinions expressed and conclusions arrived at are those of the authors and are not necessarily to be attributed to MERG. TNY Khawula thanks MERG for postgraduate bursary. K. Raju thanks the CSIR for postdoctoral fellowships. CSIR is a partner in the CREATe-Network project being funded by the European Commission under the Marie Skłodowska-Curie Actions Research and Innovation Staff Exchange (RISE).

References

1 B. E. Conway, *Electrochemical Supercapacitors, Scientific Fundamentals and Technological Applications*, Kluwer Acadamic/Plenum Publishers, New York, 1999.
2 K. J. Huang, L. Wang, Y. J. Liu, H. B. Wang, Y. M. Liu and L. L. Wang, *Electrochim. Acta*, 2013, **109**, 587.
3 G. Wang, L. Zhang and J. Zhang, *Chem. Soc. Rev.*, 2012, **41**, 797.
4 G. A. Snook, P. Kao and A. S. Best, *J. Power Sources*, 2011, **196**, 1.

5 J. M. Miller, *Energy storage technology markets and applications: Ultracapacitors in combination with lithium-ion*, IEEE XploreDOI: 10.1109/ICPE.2007.4692343: 7th International Conference on Power Electronics, April 2007.
6 Mazda 'i-ELOOP' Capacitor-Based Brake Energy Regeneration System, http://www.mazda.com/publicity/release/2011/201111/111125a.html.
7 K. J. Huang, L. Wang, Y. J. Liu, H. B. Wang, Y. M. Liu and L. L. Wang, *Int. J. Hydrogen Energy*, 2013, **38**, 14027.
8 S. Wang, C. An and J. Yuan, *Materials*, 2010, **3**, 401.
9 G. Ma, H. Peng, J. Mu, H. Huang, X. Z. Zhou and Z. Lei, *J. Power Sources*, 2013, **229**, 72.
10 M. Mandal, D. Ghosh, S. S. Kalra and C. K. Das, *Recent Res. Sci. Technol.*, 2014, **3**, 65.
11 K. Changa and W. Chen, *Chem. Commun.*, 2011, **47**, 4252.
12 K. J. Huang, L. Wang, J. Z. Zhang, L. L. Wang and Y. P. Mo, *Energy*, 2014, **67**, 234.
13 J. M. Soon and K. P. Loh, *Electrochem. Solid-State Lett.*, 2007, **10**, A250.
14 B. Hu, X. Qin, A. M. Asiri, K. A. Alamry, A. O. Al-Youbi and X. Sun, *Electrochim. Acta*, 2013, **100**, 24.
15 K. K. Moorthy, G. K. V. Subramani, S. R. Krishnan and S. J. Kim, *Mater. Res. Bull.*, 2014, **50**, 499.
16 A. N. Márquez, R. Romero, A. Romero and J. L. Valverde, *J. Mater. Chem.*, 2011, **21**, 1664.
17 T. Jiang, W. Pan, J. Wang, X. Bie, F. Du, Y. Wei, C. Wang and G. Chen, *Electrochim. Acta*, 2010, **55**, 3864.
18 K. J. Huang, L. Wang, J. Li and Y. M. Liu, *Sens. Actuators, B*, 2013, **178**, 671.
19 S. Wang, G. Li, G. Du, X. Jiang, C. Feng, Z. Guo and S. J. Kim, *Chinese J. Chem. Eng.*, 2010, **18**, 910.
20 M. W. Dlamini, D. O. Kumi, T. N. Phaahlamohlaka, A. S. Lyadov, D. G. Billing, L. L. Jewell and N. J. Coville, *ChemCatChem*, 2015, **7**, 3000.
21 F. Béguin, V. Presser, A. Balducci and E. Frackowiak, *Adv. Mater.*, 2014, **26**, 2219.
22 K. Makgopa, P. M. Ejikeme, C. J. Jafta, K. Raju, M. Zeiger, V. Presser and K. I. Ozoemena, *J. Mater. Chem. A*, 2015, **3**, 3480.
23 C. Wang, W. Wan, Y. Huang, J. Chen, H. H. Zhou and X. X. Zhang, *Nanoscale*, 2014, **6**, 5351.
24 H. Li, Q. Zhang, C. C. Ray Yap, B. K. Tay, T. H. Tong Edwin, A. Olivier and D. Baillargeat, *Adv. Funct. Mater.*, 2012, **22**, 1385.
25 G. L. Frey, R. Tenne, M. J. Matthews, M. S. Dresselhaus and G. Dresselhaus, *Phys. Rev. B: Condens. Matter Mater. Phys.*, 1999, **60**, 2883.
26 C. Lee, H. Yan, L. E. Brus, T. F. Heinz, J. Hone and S. Ryu, *ACS Nano*, 2010, **4**, 2695.
27 A. N. Mohan and B. Manoj, *Int. J. Electrochem. Sci.*, 2012, **7**, 9537.
28 M. Acerce, D. Voiry and M. Chhowalla, *Nat. Nanotechnol.*, 2015, **10**, 313.
29 M. A. Bissett, I. A. Kinloch and R. A. W. Dryfe, *ACS Appl. Mater. Interfaces*, 2015, **7**, 17388–17398.
30 D. Voiry, A. Goswami, R. Kappera, C. C. C. Silva, D. Kaplan, T. Fujita, M. Chen, T. Asefa and M. Chhowalla, *Nat. Chem.*, 2015, **7**, 45–49.
31 C. Peng, D. Hu and G. Z. Chen, *Chem. Commun.*, 2011, **47**, 4105.
32 J. B. Jorcin, M. E. Orazem, N. Pébère and B. Tribollet, *Electrochim. Acta*, 2006, **51**, 1473.